

Deep Learning Enabled Fast Optical Characterization of Two-Dimensional Materials

Bingnan Han^{1,2,†}, Yuxuan Lin^{2,†}, Yafang Yang³, Nannan Mao^{2,4}, Wenyue Li¹, Haozhe Wang², Valla Fatemi³, Lin Zhou², Joel I-Jan Wang⁵, Qiong Ma³, Yuan Cao³, Daniel Rodan-Legrain³, Ya-Qing Bie³, Efrén Navarro-Moratalla⁶, Dahlia Klein³, David MacNeill³, Sanfeng Wu³, Wei Sun Leong², Hikari Kitadai⁴, Xi Ling^{4,7}, Pablo Jarillo-Herrero^{3,*}, Tomás Palacios^{2,*}, Jihao Yin^{1,*}, Jing Kong^{2,5,*}

¹ Image Processing Center, School of Astronautics, Beihang University, Beijing 100191, China

² Department of Electrical Engineering and Computer Science, Massachusetts Institute of Technology, Cambridge, MA 02139, USA

³ Department of Physics, Massachusetts Institute of Technology, Cambridge, MA 02139, USA

⁴ Department of Chemistry, Boston University, Boston, MA 02215, USA

⁵ Research Laboratory of Electronics, Massachusetts Institute of Technology, Cambridge, MA 02139, USA

⁶ Instituto de Ciencia Molecular, Universidad de Valencia, c/Catedrático José Beltrán 2, 46980 Paterna, Spain

⁷ Division of Materials Science and Engineering, Boston University, Boston, MA 02215, USA

[†] These authors contributed equally to this work.

*Correspondence to: (J. K.) jingkong@mit.edu; (J. Y.) jihaoyin@buaa.edu.cn; (T. P.) tpalacios@mit.edu; (P. J. H.) pjarillo@mit.edu;

Abstract

Characterization of nanomaterial morphologies with advanced microscopy and/or spectroscopy tools plays an indispensable role in nanoscience and nanotechnology research^{1, 2, 3, 4, 5}, as rich information about the chemical compositions, crystallography, other physical and chemical properties, as well as the growth mechanism can be extracted from morphology analysis. However, the interpretation of imaging data heavily relies on the “intuition” of experienced researchers. As a result, many of the deep graphical features are often unused because of difficulties in processing the data and finding the correlations. Such difficulties can be well addressed by deep learning^{6, 7, 8, 9}. In this work, we use the optical characterization of two-dimensional (2D) materials as a case study, and demonstrate a neural network based algorithm for the material and thickness identification of exfoliated 2D materials with high prediction accuracy and real-time processing capability. Further analysis shows that the trained network can be used to predict physical properties of the materials. Finally, a transfer learning technique is applied to adapt the pretrained network to more optical characterization applications such as identifying layer numbers of chemically synthesized graphene domains.

Main Text

Research activities on two-dimensional (2D) materials have been exponentially growing in the past decade^{10, 11}. Up to now, hundreds of 2D materials have been isolated and studied^{11, 12, 13, 14}, offering a wide range of optical and electronics properties, including metals, semiconductors, insulators, magnets, and superconductors. The most widely used approach to obtain high-quality 2D crystals in laboratories is mechanical exfoliation^{15, 16}, followed by 2D crystal “hunting” under an optical microscope (Figure 1, left). This task is time-consuming and difficult especially for inexperienced researchers. Very recently, there has been growing interest in automating such a process¹⁷. An automatic optical identification and/or characterization system requires an algorithm that performs reliably for different materials and with different user requirements, is easily adaptable to different optical setups, and is fast enough for real-time processing. However, existing optical identification methods are completely based on optical contrast of the 2D crystals^{18, 19, 20, 21, 22, 23}, and as a result, they are often specific to types of 2D crystals, conditions and configurations of the microscopes being used, image qualities, *etc.* In addition, optical contrast based methods would fail for harder problems in which the classes to be differentiated are not separable in the color space, such as identifying the materials in unlabeled optical images (Figure S1).

In reality, optical microscopic (OM) images contain rich, often unused information other than optical contrast. These deep graphical features can be extracted through deep learning, especially semantic segmentation methods based on convolutional neural networks (CNNs)^{6, 7, 8, 9}. In this work, an encoder-decoder semantic segmentation network called “SegNet”⁹ is configured for pixel-wise identification of OM images of 2D materials. We demonstrate that this architecture can identify, in real time, various 2D materials in OM images regardless of variations in optical setups. Additionally, we find that the algorithm finds correlations between the OM images and physical

properties of the 2D materials and can thereby be used to anticipate the properties of new, as-yet uncharacterized 2D crystals.

Figure 1 illustrates the flow chart of our deep learning based optical identification method. Figures 1 (a) and (c) show 13 different 2D materials used for training, their crystal structures, photos of their bulk (three dimensional) source crystals ²⁴ and representative OM images of exfoliated 2D crystallites (or “flakes”) on top of 285 nm or 90 nm SiO₂/Si substrates. These materials are graphene/graphite, hexagonal boron nitride (hBN), the 2H-phase semiconducting transition-metal dichalcogenides (TMDs) 2H-MoS₂, 2H-WS₂, 2H-WSe₂ and 2H-MoTe₂, the 2H-phase metallic TMDs 2H-TaS₂ and 2H-NbSe₂, the 1T-phase TMD 1T-HfSe₂, black phosphorous (BP), the metal trihalides CrI₃ and RuCl₃, and the quasi-one-dimensional (quasi-1D) crystal ZrTe₅. A total number of 850 OM images containing exfoliated flakes of these 13 materials were collected and labeled for training and testing. To make the training data representative of the typical variability of OM images, the training and test data were sampled from a collection of OM images generated by at least 30 users from 8 research groups with 6 different optical microscopes over a span of 10 years. These optical images have considerable variations in brightness, contrast, white balance, and non-uniformity of the light field (Figure S2, left) because of the variations between different setups and user preferences. Note that the previously reported optical-contrast-based optical identification methods require the images to be taken in the same optical setup and with very similar hardware and software configurations ^{18, 19, 20, 21, 22, 23}. The data were labeled with the material identifications and thicknesses in a pixel-by-pixel fashion with the help of a semi-automatic image segmentation program (Figure S3 and Methods). After color normalization and data augmentation (Figure S2 and Methods), a training dataset of 22, 950 RGB images and a test dataset of 2, 550 images, both with the size of 224 by 224 pixels, were generated from the 850 OM images. A stochastic gradient

descent with momentum (SGDM) method²⁵ was used to train the weights in the convolutional filters of the SegNet. The SegNet (the schematic is shown in Figure 1 (d)) consists of a series of downsampling layers (encoder) and a corresponding set of upsampling layers (decoder) followed by a pixel-wise classifier. We select a well-known network structure called VGG16²⁶ as the encoder network in SegNet, and the detailed information about the network structure, the data generation and augmentation, as well as the network training process can be found in Figures 1 and S2, Table S1 and Methods section.

We first show that the trained SegNet can be used to segment the OM images among 13 different exfoliated 2D materials and find the material identity and thickness of each flake with good accuracy. The performance can be visualized in Figure 1, Table S2 and Figure S4. The color maps in Figure 1 (e) are the typical label maps predicted by the trained SegNet with the corresponding OM images in Figure 1 (c) as the input to the SegNet. Figure S4 shows additional results of the test OM images, the ground-truth label maps (labeled semi-automatically by humans), as well as the predicted label maps. In addition to material separability, we labeled four materials (graphene/graphite, 2H-MoS₂, 2H-WSe₂, and 2H-TaS₂) with different thicknesses (1L for monolayer, 2-6L for bilayer to 6-layer, and >6 for greater than 6 layers) to verify the thickness differentiation capability, which is a particularly important task. The trained SegNet is able to outline individual flakes from the background and distinguish both the material identities and thicknesses of the thirteen 2D materials with high success rate. Figure 2 presents the pixel-level (Figure 2 (a-e)) and the flake-level (Figure 2 (f-j)) confusion matrices of the test dataset (see Methods for more details). The diagonal elements are the success rate of each class, and the off-diagonal elements are the rate of misclassified pixels or flakes in the test OM images. The classification accuracies of material identities (Figure 2 (a) and (f)) are well above 70% and the

classification accuracies of thicknesses (Figure 2 (b-e) and (g-j)) are mostly above 60%. As shown in Table S2, the pixel-by-pixel global accuracy reaches 96.11%; the mean class accuracy is 77.98%; and the mean intersection over union (IoU, defined as the intersection of the ground truth and the predicted region of a specific label over the union of them) is 53.47% for the training dataset.

Note that the calculated performance metrics of the SegNet are likely an underestimate: after the SegNet's analysis, we discovered a number of OM images in which the ground-truth was initially mislabeled, but predicted correctly by the SegNet (Figure S5). This scenario is considered as a classification mistake in the above metrics. On the other hand, it is observed that many of the mistakes made by network are due to the similarities between different materials. For example, misclassification rates among 2H-MoS₂, 2H-WS₂, 2H-WSe₂ and 2H-MoTe₂ are as high as 8%, which is likely a consequence of their similar crystal structures and optical properties. Another type of common mistake is that metal markers, tape adhesive residue and text labels in the OM images were misidentified as a 2D material (Figure S5). These non-2D material features were labeled as “background” together with the blank substrate in the ground-truth, but they have high color contrast and other structures relative to the substrate, thereby confusing the network. In a future version of the network, this may be solved by introducing specific labels for these non-2D material features. Another common mistake is inaccuracy in the profiles of the flakes. This usually happens when the profiles are very complex, or if the flakes are highly fragmentary (Figure S5). These mistakes are mainly due to the downsampling of the encoder layers in the SegNet, which inevitably drops the high frequency spatial features of the images.

We believe that the proposed deep learning algorithm is well suited to real-time processing according to the metrics given in Table S2. With our computing environment (see Methods), the training process for the VGG16 SegNet requires 9 hours with a GPU, whereas the testing speed

can be as high as 3 frames per second (fps) using a CPU, and 20 fps using a GPU for the 224-by-224-pixel test images. This means the SegNet, once properly trained, can be easily adapted to standard desktop computers and integrated with optical microscopes with automatic scanning stages for fast or even real-time identification.

To understand how the SegNet extracts features from 2D material OM images, we analyzed the output feature maps of all the layers in the trained network for the OM images in the test dataset as the inputs. As a demonstration, we used a typical image of graphite/graphene (shown in Figure S6 (a)) as the input. The corresponding convolutional feature maps of all the layers in the encoder, decoder, and output sections of the SegNet are summarized in Figure S6 (b)-(d). Taking the convolutional feature maps in the encoder as an example (Figure S6 (b)), we can clearly see that Depth=1 feature maps are highly correlated to color and contrast information. In this shallow layer, the background and monolayer region of graphene are not easily separable because of the weak contrast between the two classes, whereas multilayer graphene region is already quite distinguishable. In Depth=2 feature maps, more boundary characteristics are detected, and the edges of graphene monolayer regions start to stand out in some of the feature maps. With the increase of the depth, the size of each feature map becomes smaller because of the pooling layers in the network, and the receptive field of each convolutional kernel (the area in the input image each neuron in the current layer can respond to) becomes relatively larger, which leads to a higher level abstraction of the global graphical features. For instance, Figure S6 (e) displays the most prominent feature map (channel #153) of the Depth=5 encoder layer with the largest activation value. It is observed that this feature map is highly correlated to the monolayer graphene region. By feeding the network with more test images as summarized in Figure S14, we further confirmed that channel #153 is sensitive to pink/ light purple flakes with smooth edges and regular shapes.

After further analysis on the 512 channels of the Depth=5 encoder layer with more test images randomly chosen from our database, we concluded that the trained SegNet is able to capture deep and subtle graphical features that were overlooked by previously reported optical contrast based approaches^{18, 19, 20, 21, 22, 23}. Many of the deep graphical features reflect in part the physical properties of the 2D materials. To illustrate this, we select 14 easily interpreted channels and discuss their associated graphical features and the related physical properties as summarized in Figure 3, Table S3, as well as Figures S7-S20. We divide the graphical features captured by these channels into four broad categories: (1) contrast or color, (2) edge or gradient, (3) shape, and (4) flake “size”. Figure 3 shows the heat maps of several channels that belong to each category. In particular, channels #153, #389 and #457 under the “contrast/color” category (Figure 3 (b)) are sensitive to flakes with purple/pink, yellow/green/grey and dark purple/dark blue colors, respectively; channels #13 and #465 under the “edge” category (Figure 3 (c)) reveal bottom and right edges, respectively; channels #153, #206 and #490 under the “shape” category (Figure 3 (e)) are indicators of shapes with edges at 60/120 degree angles, acute angles shapes and slender shapes; and channels #76 and #138 under the “flake size” category capture small or fragmentary flakes. Table S3 and Figures S7-S20 provide more details about the typical images, their corresponding heat maps as well as the extracted graphical features of the 14 channels. Note that some channels can only respond to images that meet a combinational criterion under multiple categories, whereas some channels can be sensitive to several different scenarios. For example, channel #13 only shows high intensities in the heat map around the bottom edges of purple or pink flakes (Figure S8), and channel #470 can be used to identify both non-uniform, thick flakes and uniform, thin, pale-purple flakes (Figure S19).

The above feature map analysis has provided a better understanding about how deep graphical features can be extracted by the SegNet for more accurate and generic optical identification of exfoliated 2D materials. However, the algorithm is not limited to this particular task, and we found that it can be used for more advanced optical characterization tasks such as the prediction of material properties. The graphical features captured by the network are correlated to the optical and mechanical properties of the material. As shown schematically in Figure 3 (a), the contrast/color and the edge features are determined by the optical response of the material, which reflect the electronic band structures and the thicknesses of the flakes. In addition, because the samples were made through mechanical exfoliation, the typical distribution of shapes and sizes of the flakes depends heavily on the mechanical properties of the materials, such as the crystal symmetry, mechanical anisotropy and the exfoliation energy (Figure 3 (d)). We can thus use the trained network with the knowledge of the 13 materials to predict properties of unstudied materials. One simple approach to implement the material property predictor is to take the “similarity” vectors of each material from the confusion matrix (each row of the matrix) and decompose the vectors to a set of specifically designed base vectors. In this way, the projected values can give us a probabilistic prediction of the physical property of interest (more details are given in the Methods section). As a proof-of-concept demonstration, we fed the trained network with OM images of 17 2D materials that were unknown to the network during the training stage. The extended confusion matrix containing the 13 trained materials and the 17 untrained materials is shown in Figure S21, and the physical properties of these 2D materials are summarized in Table S4. As we can see, different vector components in the similarity vectors (or columns of the extended confusion matrix) have distinct values for each of the untrained materials, from which we can immediately summarize some qualitative patterns. For example, GaS, CrI₃, CrBr₃ and MnPS₃ in the untrained

material group shows high similarity to hBN in the trained material group, which matches the fact that these materials are wide-bandgap semiconductors or insulators with the band gaps higher than 2.5 eV and are mostly transparent in the infrared, red and green spectral ranges. As another example, 1T'-MoTe₂ and Td-WTe₂ in the untrained material group are predicted to be similar to 1T-HfSe₂ in the trained material group, which is in accordance with the similar crystal structure of these materials. For a more quantitative analysis, we selected two different predictors that are associated with the band gaps and the crystal structures of the material, and the projected values of each material based on these two predictors are plotted into a histogram and summarized in Figure 4 (a) and (b), respectively. Clear correlations between the projected values and the true physical parameters (band gap in Figure 4 (a), and crystal structure in Figure 4 (b)) are found. We can thus use the projected values as an indication of the probability of the physical property of interest of an unknown material belonging to each classes (represented by each base vector of the corresponding predictor). Note that there are also misclassified instances, which we believe can be improved by expanding the training data set in terms of both the number of images and the number of materials. This method can potentially be used for systematic studies of other factors such as the effect of different mechanical exfoliation techniques, bulk crystal qualities, and so on.

Finally, we demonstrate that the trained SegNet can be adapted for different applications through transfer learning. The basic idea is to use the trained SegNet as the initialization for the new training problem rather than a random initialization. With this approach, we are able to train the SegNet for new optical identification/characterization problems with minimal extra computation time and data for the training. Here we use OM images of graphene synthesized by chemical vapor deposition (CVD) as a demonstration. Figure 5 (a) shows the test images, the ground truth label maps as well as the corresponding prediction results after the training with the transfer learning

approach. As we can see, the prediction results match the ground truths very well. To compare the pre-training transfer learning approach with the conventional approach with random initialization, we plot the global test accuracy of networks trained with both approaches as a function of the number of OM images in the training data set as shown in Figure 5 (b). Representative test images and their predictions can be found in Figure S22. With the pre-training approach, we were able to achieve 65% global accuracy with only 30 training images, whereas at least 60 images are required for the conventional random initialization approach to reach comparable accuracy.

In summary, we develop a deep learning algorithm for the optical characterization of 2D materials and the extraction of deep graphical features from optical microscopic images that can be used for anticipating material properties. After training, the neural network can achieve rapid characterization of material identities, their thicknesses and physical properties with good accuracy. A fully automated system utilizing this algorithm can be used to free up tremendous amount of time for researchers. A systematic analysis was made to understand how the network captures deep graphical features such as color, contrast, edges, shapes and flakes sizes from the optical images. We also demonstrate that the trained network can be adapted for different optical characterization applications with minimal additional training through a transfer learning technique. The proposed methodology can potentially be extended for identification and understanding other morphological or spectroscopic data of diverse nanomaterials.

Methods

Constructing, Training and Testing the SegNet

(1) Network structure

The SegNet-based optical identification process is summarized in Figure 1 and Figure S2. The SegNet consists of a series of downsampling layers (encoder) and a corresponding set of up sampling layers (decoder) followed by a pixel-wise classifier. As an end-to-end network, the SegNet can predict labels of 2D materials at the pixel level, and the size of the output label map is exactly the same as the input optical microscope image. This can help us directly identify the material identities and the thicknesses of individual 2D material flakes. We select a well-known network structure VGG16²⁶ as the basis of the encoder network in the SegNet. Table S1 summarizes the VGG16 network structure. The encoder contains a stack of convolutional layers which have 3 by 3 receptive field and pixel stride 1, followed by a batch normalization and a nonlinear activation (ReLU) layer. Then a max-pooling layer with a 2 by 2 window and stride 2 is applied for the image downsampling. The decoder net and the encoder net are symmetric. The only difference between them is that in decoder we use an upsampling layer to replace max-pooling layer. The indices in upsampling layers are grabbed directly from the indices of the corresponding max-pooling layers. In this way, the locations of the poolings are memorized and recovered in the upsampling layers, which improves the spatial accuracy of the network. Finally, a soft-max classifier is added at the end of the network for pixel-wise classifications. The output label maps have the same dimension as the input OM images.

(2) Data generation

There are 3 steps to generate the pixel-wise labeled dataset for the training of the SegNet: labeling, color normalization, and data augmentation.

To generate pixel-wise labeled OM images for the training and testing, we used a semi-automatic graph-cut method implemented by MATLAB. Graph-cut is a traditional semantic segmentation method based on graph theory²⁷. Although the initial segmentation performance of this method is poor, we can promote the performance by adding human assistance. By drawing loosely the foreground regions and the background regions, the algorithm can find the boundary of the segment of interest with good accuracy. Figure S3 demonstrate the labeling procedure under human-assisted graph-cut method.

We select thirteen 2D materials as experiment samples. They are graphene/graphite, hexagonal boron nitride (hBN), 2H-MoS₂, 2H-WS₂, 2H-WSe₂, 2H-MoTe₂, 2H-TaS₂, 2H-NbSe₂, 1T-HfSe₂, black phosphorous (BP), CrI₃, RuCl₃ and ZrTe₅. 100 images for each of Graphene/Graphite, 2H-MoS₂, 2H-WS₂ and 2H-TaS₂ were labeled with three classes (“monolayer”, “fewlayer (2-6L)” and “multilayer (>6L)”) to demonstrate the thickness identification capabilities, and 50 images for each of the other 9 materials were labeled with only single classes. The total number of classes (including background) is 22, and the total number of labeled OM images is 850.

To partially reduce the color-related variations of the OM images because of different setups and user preferences, a color normalization was performed on all the images. We first converted the RGB images into the Lab color space, and the following transformation was applied to all the pixels: $L \leftarrow 30L/L_{\text{ref}}$, $a \leftarrow a - a_{\text{ref}}$, and $b \leftarrow b - b_{\text{ref}}$, where L_{ref} , a_{ref} and b_{ref} are the Lab values of the background obtained by finding the median L , a and b of each image. The resulting Lab images were then converted back to RGB images.

After labeling and color normalization, we selected 90% of the labeled images as the training dataset, and 10% as the test dataset. The original images were first resized and chopped into 224 by 224 pixel images, then a data augmentation strategy is applied to provide more training examples to the network and thus to improve the accuracy of the network. Each chopped image was flipped (horizontal and vertical) and rotated (by 0°, 90°, 180° and 270°) to generate 6 augmented images. Finally, we obtained 22, 950 images in the training dataset and 2, 550 images in the test dataset.

(3) Training and testing

The training and testing of the SegNet were implemented in *MATLAB R2018b* with the help of the *Deep Learning Toolbox*, the *Parallel Computing Toolbox*, the *Computer Vision Toolbox* and the *Image Processing Toolbox*. The training and testing were performed using a desktop computer equipped with a CPU (Intel(R) Core (TM) i7-8700K @ 3.70GHz, 32.0GB RAM) and a GPU (NVIDIA GeForce GTX 1080 Ti, 11 GB GDDR5X). The stochastic gradient descent with momentum (SGDM) method²⁵ was used to find the weights in the convolutional filters of the SegNet during the training process. To compensate for the imbalanced numbers of pixels for different classes (for example, the “background” labels take more than 85% of areas in most images), class weightings based on inverse frequencies were used in the soft-max classifier.

Confusion Matrices and Material Property Predictors

The confusion matrices (Figure 2 and Figure S21) were obtained by using the OM images in the test dataset as the input of the trained SegNet and comparing the corresponding output label maps with the ground truth label maps. For example, the element on i -th row and j -th column corresponds to the fraction of the i -th class that are labeled as the j -th class by the SegNet. We also

present two types of confusion matrices: the pixel-level confusion matrices (Figure 2 (a)-(e), and Figure S21) and the flake-level confusion matrices (Figure 2 (f)-(j)). For the pixel-level confusion matrices, the matrix elements are the ratio counted pixel by pixel, whereas the flake-level confusion matrices take the majority label of all the pixels in each segmentation, or “flake”, as the label of the flake and calculated the fraction based on the flake labels. Note that the flake labels ignored any segmentations with fewer than 100 pixels, because they are either fractures on the edges of the actual 2D crystal flakes, or some non-uniform regions on the background.

To demonstrate the SegNet’s capability of predicting physical properties of unknown 2D materials, we also fed the trained SegNet with additional OM images of new 2D materials that were not used in the training dataset, and calculated the “extended” confusion matrix as shown in Figure S21. The new materials include 2H-MoSe₂, 1T’-MoTe₂, Td-WTe₂, ReS₂, SnS₂, SnSe₂, GeSe, SnSe, GaS, CrCl₃, CrBr₃, MnPS₃, FePS₃, TiS₃, ZrS₃, Bi₄I₄ and Ta₂Se₈I. The row vectors in the extended confusion matrix can be used to characterize how similar the physical properties of one material are to the 13 known materials. Therefore, we can use these “similarity” vectors to extract information about physical properties of a new material. A very simple way of constructing such physical property predictors is to project the “similarity” vectors in a set of base vectors that are correlated to the physical property of interest. We can define each base vector as the average of the vectors of the known materials that have the same value or range of the physical property of interest, expressed as $\mathbf{v}_k = (\sum_{x \in \mathbf{M}_k} \mathbf{v}_x) / \|\mathbf{M}_k\|$, where \mathbf{v}_k is the base vector of the k -th class in the material property predictor; \mathbf{v}_x is the base vector of the material x in the training set; \mathbf{M}_k is the subset of materials in the training set that have matched criteria of the physical properties in the k -th class in the predictor; and $\|\mathbf{M}_k\|$ is the number of materials in the \mathbf{M}_k subset. For the band gap

predictor, the base vector subsets are $\mathbf{M}_1=\{\text{Graphene/Graphite}, 2\text{H-TaS}_2, 2\text{H-NbSe}_2, \text{ZrTe}_5, \text{BP}, 2\text{H-MoTe}_2, 1\text{T-HfSe}_2, \text{RuCl}_3, \text{CrI}_3\}$, $\mathbf{M}_2=\{2\text{H-MoS}_2, 2\text{H-WSe}_2, 2\text{H-WS}_2\}$, $\mathbf{M}_3=\{\text{hBN}\}$; for the crystal structure predictor, the base vector subsets are $\mathbf{M}_1=\{\text{Graphene/Graphite}, \text{hBN}, 2\text{H-MoS}_2, 2\text{H-WSe}_2, 2\text{H-WS}_2, 2\text{H-MoTe}_2, 2\text{H-TaS}_2, 2\text{H-NbSe}_2\}$, $\mathbf{M}_2=\{1\text{T-HfSe}_2\}$, $\mathbf{M}_3=\{\text{BP}\}$, $\mathbf{M}_4=\{\text{RuCl}_3, \text{CrI}_3\}$, $\mathbf{M}_5=\{\text{ZrTe}_5\}$. A summary of physical properties of the 2D materials being used in this study can be found in Table S4.

Transfer Learning for Small Amount of Training Data

In the transfer learning experiment, we only labeled 5 OM images of CVD grown graphene, and generate 600 images (224 by 224 pixels) by data augmentation. We divided the graphene region into five classes based on its layer number (from monolayer to 5-layers). We varied the size of the training dataset from 30 to 360, and sampled randomly from the 600 images. For the transfer learning, the initial weights in the network before the training are taken from the pretrained SegNet (trained with the 13 exfoliated 2D materials) as compared to the conventional random initialization strategy.

Acknowledgement

This material is based upon work sponsored in part by the U.S. Army Research Office through the Institute for Soldier Nanotechnologies, under cooperative agreement number W911NF-18-2-0048, AFOSR FATE MURI, grant no. FA9550-15-1-0514, National Natural Science Foundation of China (grant no. 41871240), the National Science Foundation grant 2DARE (EFRI-1542815), NSF DMR-1507806, and the STC Center for Integrated Quantum Materials, NSF Grant No. DMR-5991231319. Work by the P. J. H. group was primarily funded by the DOE Office of Science, BES,

under award DE-SC0019300. B. H. gratefully acknowledges the financial support from China Scholarship Council.

Author Contributions

Y.L., Y.Y., B. H., J. Y. and J. K. conceived the experiment. B. H., Y. L., Y. Y. and W. L. performed the training and testing of the SegNet. B. H., Y. Y., N. M. Y. L. and H. W. carried on the data labeling. B. H. and Y. L. did further analysis of the trained network. N. M., Y. Y., Y. L., H. W., L. Z., J. I-J. W., Q. M., J. L., Y. C., D. R.-L., Y. B, E. N.-M., D. K., D. M., V. F., S. W., W. S. L., H. K. and X. L. provided the microscopic images. J. K., J. Y., P. J.-H. and T. P supervised this work. Y. L., B. H., Y. Y., T. P., P. J.-H., J. Y. and J. K. co-wrote the paper with inputs from all the authors.

Figures and Captions

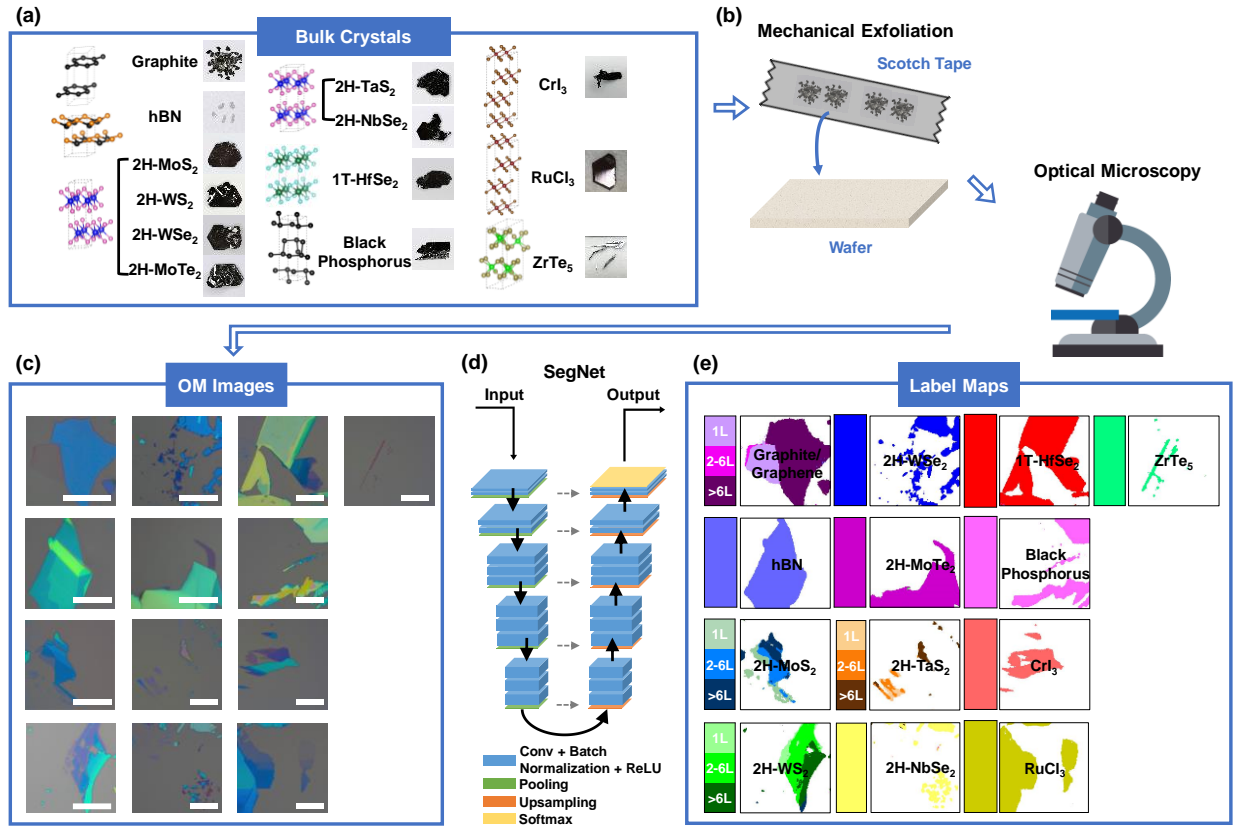


Figure 1. The flow chart of the proposed deep learning based optical identification method. We select 13 typical 2D materials (crystal structure and photographs²⁴ of the bulk crystals are shown in panel (a)). After mechanical exfoliation, the 2D flakes are randomly distributed on SiO₂/Si substrates. We then use optical microscopes to take the images (b). Panel (c) shows representative optical microscopic (OM) images of the 13 materials. When inputting these images to the trained SegNet (as shown in (d)), the label maps (e) will be predicted that segment individual 2D flakes and provide the labels (materials identities and thicknesses) of them. The SegNet is composed of a series of convolutional layers, batch normalization layers, ReLU layers (in blue), pooling (downsampling) layers (in green), upsampling layers (in orange), as well as a soft-max layer (in yellow) as the output layer. Note that the OM images displayed here and in Figures 3 and 5 are

the original high-resolution images. The images for the input of the SegNet were downsampled to 224 by 224 pixels, which can be found in Figures S4, S7-S20 and S22. Scale bars in (c), 20 μm .

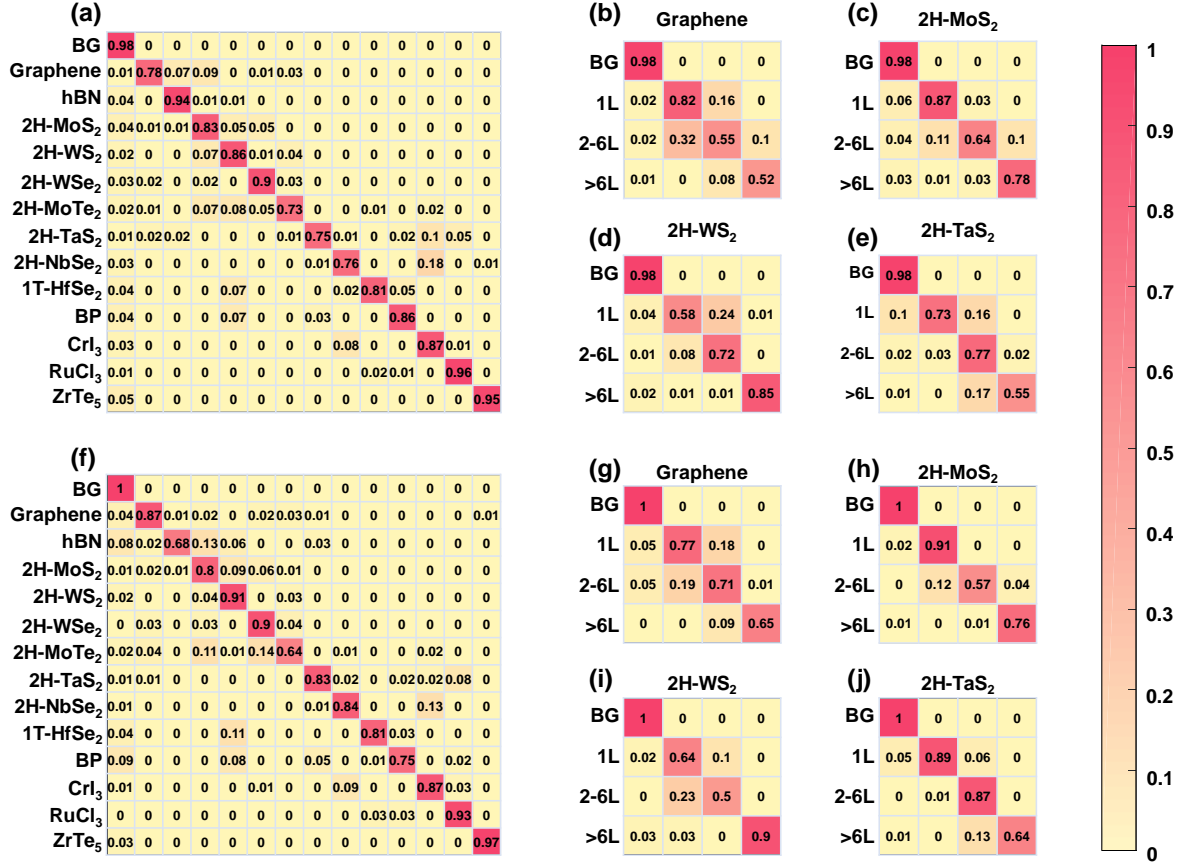


Figure 2. Confusion matrices calculated from the test results. (a)-(e) are pixel-level confusion matrices, and (f)-(j) are flake-level confusion matrices (see Methods). (a) and (f) are for material identities. (b)-(e) and (g)-(j) are for thicknesses. In each confusion matrix, the diagonal terms are the success rate of the predicted classes, and the non-diagonal terms are the rate of misclassified pixels. The prediction accuracies for the material identities are well above 70%, and the prediction accuracies for the thicknesses are mostly above 60%.

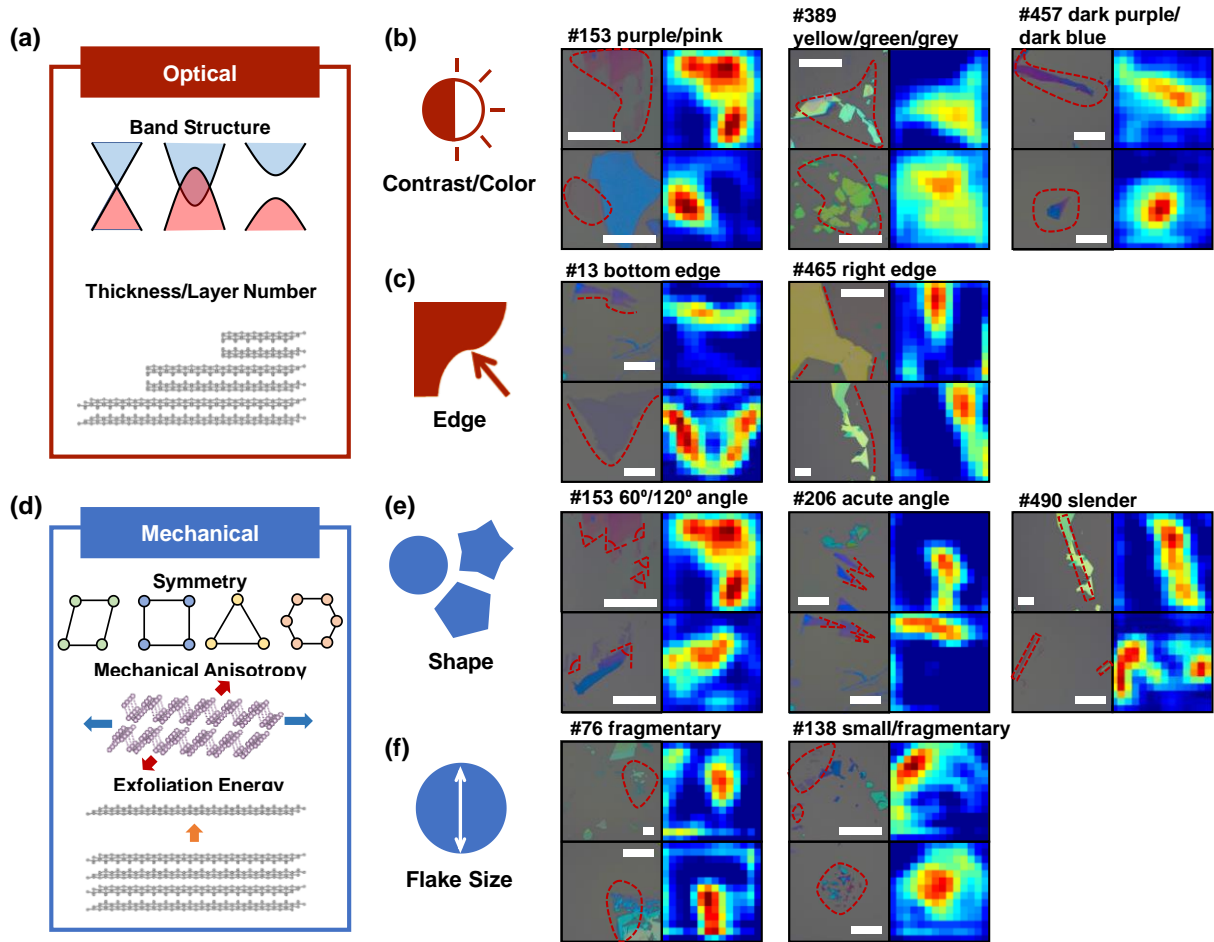


Figure 3. Deep graphical features captured by the SegNet. (a) schematics of the physical properties such as the band structure and the thickness that determine the optical responses of the 2D flakes. (b) Contrast/color and (c) edge and typical feature maps in the Depth=5 layer of the SegNet that are associated with the optical responses. (d) schematics of the physical properties such as the crystal symmetry, the mechanical anisotropy and the exfoliation energy that determine the mechanical responses of the 2D flakes. (e) flake shape and (f) flake size and typical feature maps in the Depth=5 layer of the SegNet that are correlated to the mechanical properties of the materials. The high-activation regions in the feature maps are also indicated by red dashed curves in the corresponding OM images. Scale bars: 20 μm

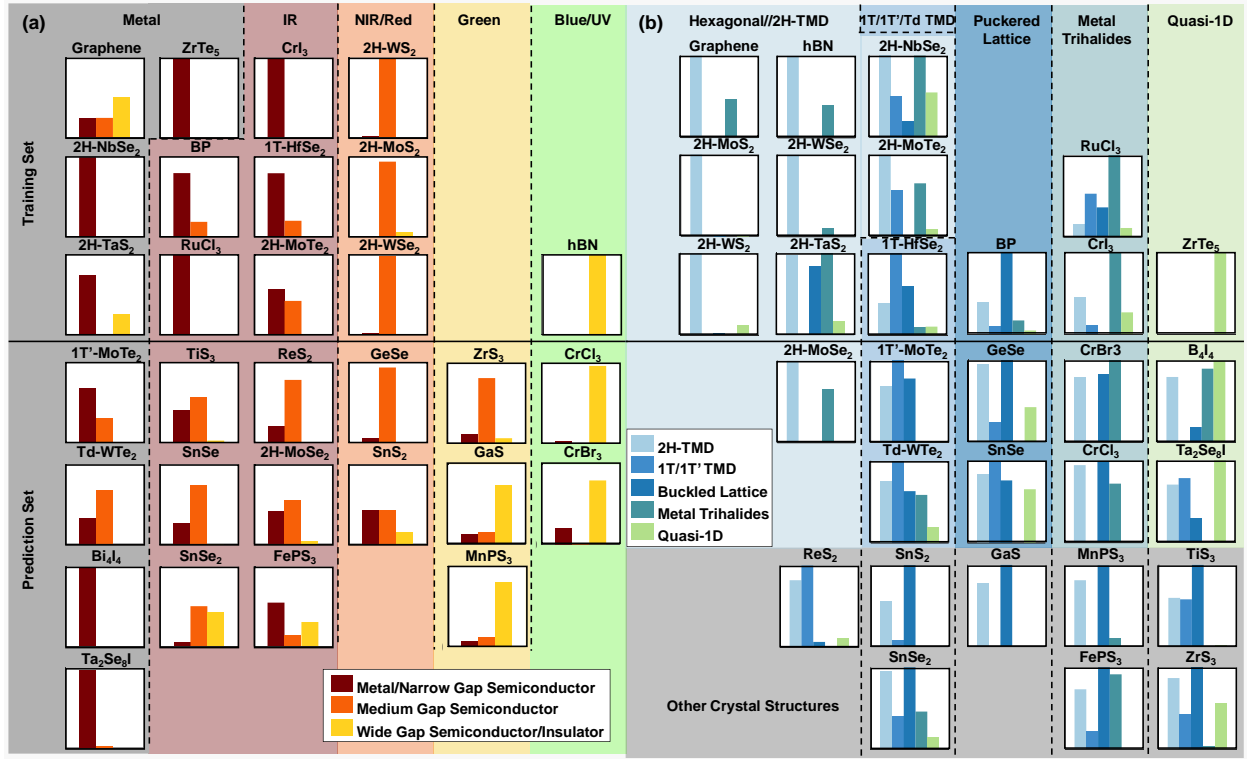


Figure 4. Prediction of physical properties based on the similarity vectors produced by the SegNet. (a) histograms of the projected values of the materials in the training set (top half) and in the prediction set (bottom half, unused when training the SegNet) that predict the bandgap of the materials. (b) histograms of the projected values that predict the crystal structure of the materials. The materials are regrouped by the bandgaps and the crystal structures respectively in (a) and (b). The training set contains the 13 materials used for the training of the SegNet, whereas the prediction set contains 17 additional materials that are unknown to the SegNet during the training stage. The materials in the grey box in (b) do not belong to any of the crystal structure classes.

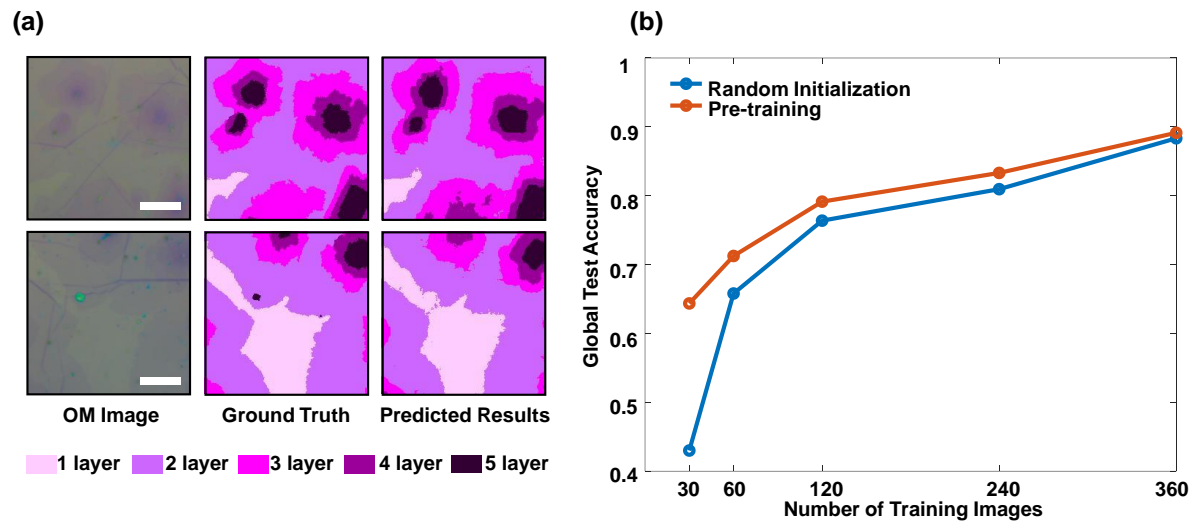


Figure 5. Transfer learning for CVD graphene. (a) Typical training results with 360 images in the training dataset. The left column are OM images, the middle column are the ground truth label maps, and the right column are the label maps predicted by the re-trained SegNet. Scale bars: 20 μm . (b) Global test accuracy as a function of the number of images in the training dataset for the pre-training method (red) and the random initialization method (blue).

Reference

1. Yao N, Wang ZL. *Handbook of microscopy for nanotechnology*. Springer, 2005.
2. van den Bos KHW, Altantzis T, De Backer A, Van Aert S, Bals S. Recent breakthroughs in scanning transmission electron microscopy of small species. *Advances in Physics: X* 2018, **3**(1): 1480420.
3. Rotenberg N, Kuipers L. Mapping nanoscale light fields. *Nature Photonics* 2014, **8**: 919.
4. Verma P. Tip-Enhanced Raman Spectroscopy: Technique and Recent Advances. *Chemical Reviews* 2017, **117**(9): 6447-6466.
5. Gross L. Recent advances in submolecular resolution with scanning probe microscopy. *Nature Chemistry* 2011, **3**: 273.
6. Long J, Shelhamer E, Darrell T. Fully convolutional networks for semantic segmentation. 2015 IEEE Conference on Computer Vision and Pattern Recognition (CVPR); 2015 7-12 June 2015; 2015. p. 3431-3440.
7. Chen L, Papandreou G, Kokkinos I, Murphy K, Yuille AL. DeepLab: Semantic Image Segmentation with Deep Convolutional Nets, Atrous Convolution, and Fully Connected CRFs. *IEEE Transactions on Pattern Analysis and Machine Intelligence* 2018, **40**(4): 834-848.
8. Ronneberger O, Fischer P, Brox T. U-Net: Convolutional Networks for Biomedical Image Segmentation. In: Navab N, Hornegger J, Wells WM, Frangi AF, editors. Medical Image Computing and Computer-Assisted Intervention – MICCAI 2015; 2015 2015//; Cham: Springer International Publishing; 2015. p. 234-241.
9. Badrinarayanan V, Kendall A, Cipolla R. SegNet: A Deep Convolutional Encoder-Decoder Architecture for Image Segmentation. *IEEE Transactions on Pattern Analysis and Machine Intelligence* 2017, **39**(12): 2481-2495.
10. Geim AK, Novoselov KS. The rise of graphene. *Nature Materials* 2007, **6**: 183.
11. Ferrari AC, Bonaccorso F, Fal'ko V, Novoselov KS, Roche S, Bøggild P, *et al.* Science and technology roadmap for graphene, related two-dimensional crystals, and hybrid systems. *Nanoscale* 2015, **7**(11): 4598-4810.
12. Nicolosi V, Chhowalla M, Kanatzidis MG, Strano MS, Coleman JN. Liquid Exfoliation of Layered Materials. *Science* 2013, **340**(6139): 1226419.

13. Wang QH, Kalantar-Zadeh K, Kis A, Coleman JN, Strano MS. Electronics and optoelectronics of two-dimensional transition metal dichalcogenides. *Nature Nanotechnology* 2012, **7**: 699.
14. Tan C, Cao X, Wu X-J, He Q, Yang J, Zhang X, *et al.* Recent Advances in Ultrathin Two-Dimensional Nanomaterials. *Chemical Reviews* 2017, **117**(9): 6225-6331.
15. Novoselov KS, Geim AK, Morozov SV, Jiang D, Zhang Y, Dubonos SV, *et al.* Electric Field Effect in Atomically Thin Carbon Films. *Science* 2004, **306**(5696): 666-669.
16. Yi M, Shen Z. A review on mechanical exfoliation for the scalable production of graphene. *Journal of Materials Chemistry A* 2015, **3**(22): 11700-11715.
17. Masubuchi S, Morimoto M, Morikawa S, Onodera M, Asakawa Y, Watanabe K, *et al.* Autonomous robotic searching and assembly of two-dimensional crystals to build van der Waals superlattices. *Nature Communications* 2018, **9**(1): 1413.
18. Li H, Wu J, Huang X, Lu G, Yang J, Lu X, *et al.* Rapid and Reliable Thickness Identification of Two-Dimensional Nanosheets Using Optical Microscopy. *ACS Nano* 2013, **7**(11): 10344-10353.
19. Lin X, Si Z, Fu W, Yang J, Guo S, Cao Y, *et al.* Intelligent identification of two-dimensional nanostructures by machine-learning optical microscopy. *Nano Research* 2018, **11**(12): 6316-6324.
20. Masubuchi S, Machida T. Classifying optical microscope images of exfoliated graphene flakes by data-driven machine learning. *npj 2D Materials and Applications* 2019, **3**(1): 4.
21. Ni ZH, Wang HM, Kasim J, Fan HM, Yu T, Wu YH, *et al.* Graphene Thickness Determination Using Reflection and Contrast Spectroscopy. *Nano Letters* 2007, **7**(9): 2758-2763.
22. Nolen CM, Denina G, Teweldebrhan D, Bhanu B, Balandin AA. High-Throughput Large-Area Automated Identification and Quality Control of Graphene and Few-Layer Graphene Films. *ACS Nano* 2011, **5**(2): 914-922.
23. Blake P, Hill EW, Castro Neto AH, Novoselov KS, Jiang D, Yang R, *et al.* Making graphene visible. *Applied Physics Letters* 2007, **91**(6): 063124.
24. [cited]Available from: <https://www.2dsemiconductors.com/>; <http://www.hqgraphene.com/>
25. Sutskever I, Martens J, Dahl G, Hinton G. On the importance of initialization and momentum in deep learning. International conference on machine learning; 2013; 2013. p. 1139-1147.
26. Simonyan K, Zisserman A. Very deep convolutional networks for large-scale image recognition. *arXiv preprint arXiv:14091556* 2014.

27. Boykov YY, Jolly M. Interactive graph cuts for optimal boundary & region segmentation of objects in N-D images. Proceedings Eighth IEEE International Conference on Computer Vision. ICCV 2001; 2001 7-14 July 2001; 2001. p. 105-112 vol.101.

Supplementary Information

Deep Learning Enabled Fast Optical Characterization of Two-Dimensional Materials

Bingnan Han^{1,2, †}, Yuxuan Lin^{2, †}, Yafang Yang³, Nannan Mao^{2,4}, Wenyue Li¹, Haozhe Wang², Valla Fatemi³, Lin Zhou², Joel I-Jan Wang⁵, Qiong Ma³, Yuan Cao³, Daniel Rodan-Legrain³, Ya-Qing Bie³, Efrén Navarro-Moratalla⁶, Dahlia Klein³, David MacNeill³, Sanfeng Wu³, Wei Sun Leong², Hikari Kitadai⁴, Xi Ling^{4,7}, Pablo Jarillo-Herrero^{3,*}, Tomás Palacios^{2,*}, Jihao Yin^{1,*}, Jing Kong^{2,5,*}

¹ Image Processing Center, School of Astronautics, Beihang University, Beijing 100191, China

² Department of Electrical Engineering and Computer Science, Massachusetts Institute of Technology, Cambridge, MA 02139, USA

³ Department of Physics, Massachusetts Institute of Technology, Cambridge, MA 02139, USA

⁴ Department of Chemistry, Boston University, Boston, MA 02215, USA

⁵ Research Laboratory of Electronics, Massachusetts Institute of Technology, Cambridge, MA 02139, USA

⁶ Instituto de Ciencia Molecular, Universidad de Valencia, c/Catedrático José Beltrán 2, 46980 Paterna, Spain

⁷ Division of Materials Science and Engineering, Boston University, Boston, MA 02215, USA

[†] These authors contributed equally to this work.

*Correspondence to: (J. K.) jingkong@mit.edu; (J. Y.) jihaoyin@buaa.edu.cn; (T. P.) tpalacios@mit.edu; (P. J. H.) pjarillo@mit.edu;

This document contains:

Tables S1-S4

Figures S1-S22

Table S1. Detailed information of the SegNet based on the VGG16 network.

	Encoder	Decoder
	Input	Output
	224*224 RGB image	Softmax
Depth=1	Conv 3*3*64 Conv 3*3*64 Maxpooling	Conv 3*3*64 Conv 3*3*64 Upsampling 2*2
Depth=2	Conv 3*3*128 Conv 3*3*128 Maxpooling 2*2	Conv 3*3*128 Conv 3*3*128 Upsampling 2*2
Depth=3	Conv 3*3*256 Conv 3*3*256 Conv 3*3*256 Maxpooling 2*2	Conv 3*3*256 Conv 3*3*256 Conv 3*3*256 Upsampling 2*2
Depth=4	Conv 3*3*512 Conv 3*3*512 Conv 3*3*512 Maxpooling 2*2	Conv 3*3*512 Conv 3*3*512 Conv 3*3*512 Upsampling 2*2
Depth=5	Conv 3*3*512 Conv 3*3*512 Conv 3*3*512 Maxpooling 2*2	Conv 3*3*512 Conv 3*3*512 Conv 3*3*512 Upsampling 2*2

Table S2. Overall classification performance of the SegNet. The experiment environment is: CPU: Intel(R) Core(TM) i7-8700K CPU @ 3.70GHz, 32.0GB RAM; GPU: NVIDIA GeForce GTX 1080 Ti, 11 GB GDDR5X.

Metrics	Global Accuracy (by pixel)	Mean Accuracy (by class)	Mean IoU (by pixel)	Training Time	Frames Per Second (FPS) in Test	
					Use CPU	Use GPU
Accuracy	0.9611	0.7798	0.5347	8 hr 40 min 9 s	2.6	20.2

Table S3. A summary of selected channels and their interpretations in the Depth=5 encoder layer of the trained SegNet.

Channel #	Cases	Contrast/Color	Edge	Shape	Flake Size
8	-	Purple/pink/dark blue			
13	-	Purple/pink	Bottom edges		
69	Case 1				Fragmentary
	Case 2			Acute angle	
	Case 3	Non-uniform			
76	Case 1				Fragmentary
	Case 2			Slender	
103	Case 1	Purple/pink			Small
	Case 2			Slender	
129	Case 1	Purple/pink	All edges		

	Case 2	Purple/pink		Slender	
138	-				Small/Fragmentary
153	-	Purple/pink	Straight/smooth edges	60°/120° angles	
206	-	Purple/ blue		Acute angle	
389	-	Yellow/green/grey			
457	-	Dark purple/dark blue			
465	-		Right edges		
470	Case 1	Non-uniform			
	Case 2	Pale purple			
490	-			Slender	

Table S4. A summary of the physical properties of the 2D materials (bulk) used in this study ^{1, 2, 3, 4, 5, 6, 7, 8, 9, 10, 11, 12, 13, 14, 15, 16, 17}. The values for the optical bandgap the direct bandgap, or the lowest peak energy in the optical absorption spectra.

Material	Crystal System	Point Group	Space Group	Bandgap (Optical)	Exfoliation Energy
graphite	Hexagonal	D _{6h}	P6/mmm	0 eV	70.36 meV
hBN	Hexagonal	D _{6h}	P6 ₃ /mmc	~6 eV	71.34 meV
2H-MoS ₂	Hexagonal	D _{6h}	P6 ₃ /mmc	1.8 eV	76.99 meV
2H-WS ₂	Hexagonal	D _{6h}	P6 ₃ /mmc	2.1 eV	76.27 meV
2H-WSe ₂	Hexagonal	D _{6h}	P6 ₃ /mmc	1.7 eV	79.63 meV
2H-MoTe ₂	Hexagonal	D _{6h}	P6 ₃ /mmc	1.1 eV	90.98 meV
2H-TaS ₂	Hexagonal	D _{6h}	P6 ₃ /mmc	0 eV	87.15 meV
2H-NbSe ₂	Hexagonal	D _{6h}	P6 ₃ /mmc	0 eV	98.28 meV
1T-HfSe ₂	Trigonal	D _{3d}	P $\bar{3}$ m1	1.1 eV	92.05 meV
BP	Orthorhombic	D _{2h}	Cmce	0.35 eV	111.62 meV
CrI ₃	Monoclinic	C _{2h}	C2/m	1.2 eV	-
RuCl ₃	Monoclinic	C _{2h}	C2/m	0.3 eV	-
ZrTe ₅	Orthorhombic	D _{2h}	Cmcm	0 eV	90.00 meV
2H-MoSe ₂	Hexagonal	D _{6h}	P6 ₃ /mmc	1.5 eV	80.24 meV
1T'-MoTe ₂	Monoclinic	C _{2h}	P2 ₁ /m	0 eV	86.87 meV
Td-WTe ₂	Orthorhombic	C _{2v}	Pmn2 ₁	0 eV	84.90 meV
GeSe	Orthorhombic	D _{2h}	Pnma	2.1 eV	-
SnSe	Orthorhombic	D _{2h}	Pnma	1.3 eV	152.65 meV
CrBr ₃	Monoclinic	C _{2h}	C2/m	3.2 eV	-
CrCl ₃	Monoclinic	C _{2h}	C2/m	3.1 eV	69.52 meV
Bi ₄ I ₄	Monoclinic	C _{2h}	C2/m	0.04 eV	77.69 meV
Ta ₂ Se ₈ I	Tetragonal	D ₄	I422	0 eV	-
GaS	Hexagonal	D _{6h}	P6 ₃ /mmc	2.5 eV	56.22 meV
ReS ₂	Triclinic	C _i	P $\bar{1}$	1.4 eV	71.00 meV
SnS ₂	Trigonal	D _{3d}	P $\bar{3}$ m1	2.4 eV	83.28 meV
SnSe ₂	Trigonal	D _{3d}	P $\bar{3}$ m1	1.6 eV	93.47 meV
MnPS ₃	Monoclinic	C _{2h}	C2/m	2.8 eV	-
FePS ₃	Monoclinic	C _{2h}	C2/m	1.5 eV	-
TiS ₃	Monoclinic	C _{2h}	P2 ₁ /m	1.1 eV	54.49 meV
ZrS ₃	Monoclinic	C _{2h}	P2 ₁ /m	2.5 eV	55.49 meV

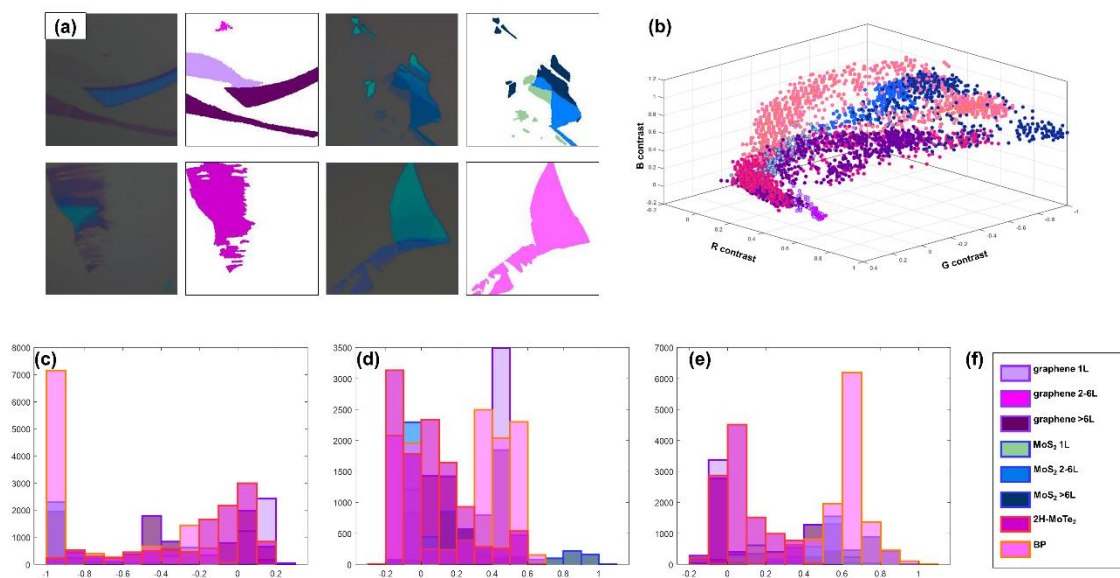


Figure S1. Optical contrast analysis of 4 different 2D materials, including graphene, MoS₂, 2H-MoTe₂, and BP. (a) typical OM images and the corresponding ground truth label maps. (b) RGB distribution of the images in (a). (c) Distribution of R values, (d) distributions of G values, and (e) distribution of B values of the images in (a). (f) color scales.

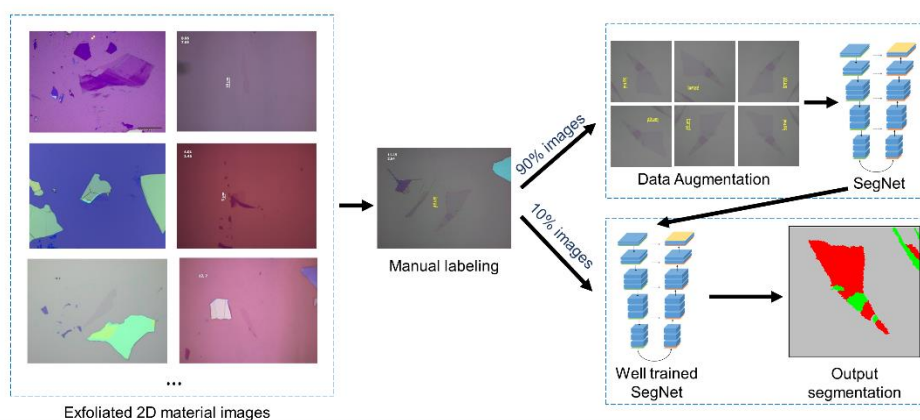


Figure S2. Schematic of the data generation procedure.

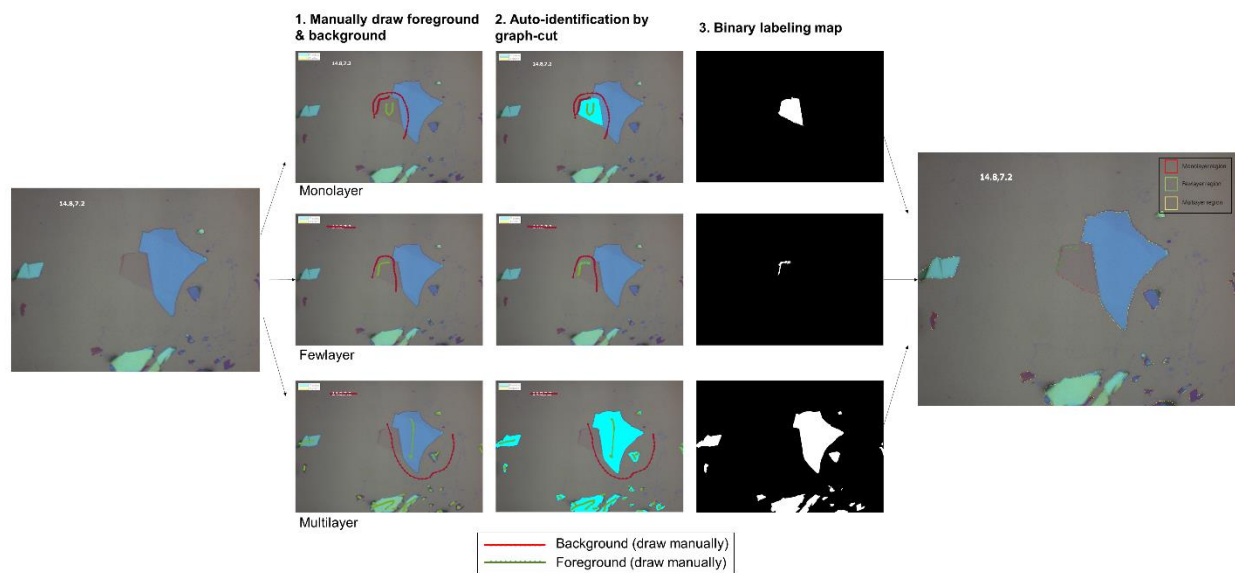


Figure S3. Schematic of the semi-automatic labeling procedure.

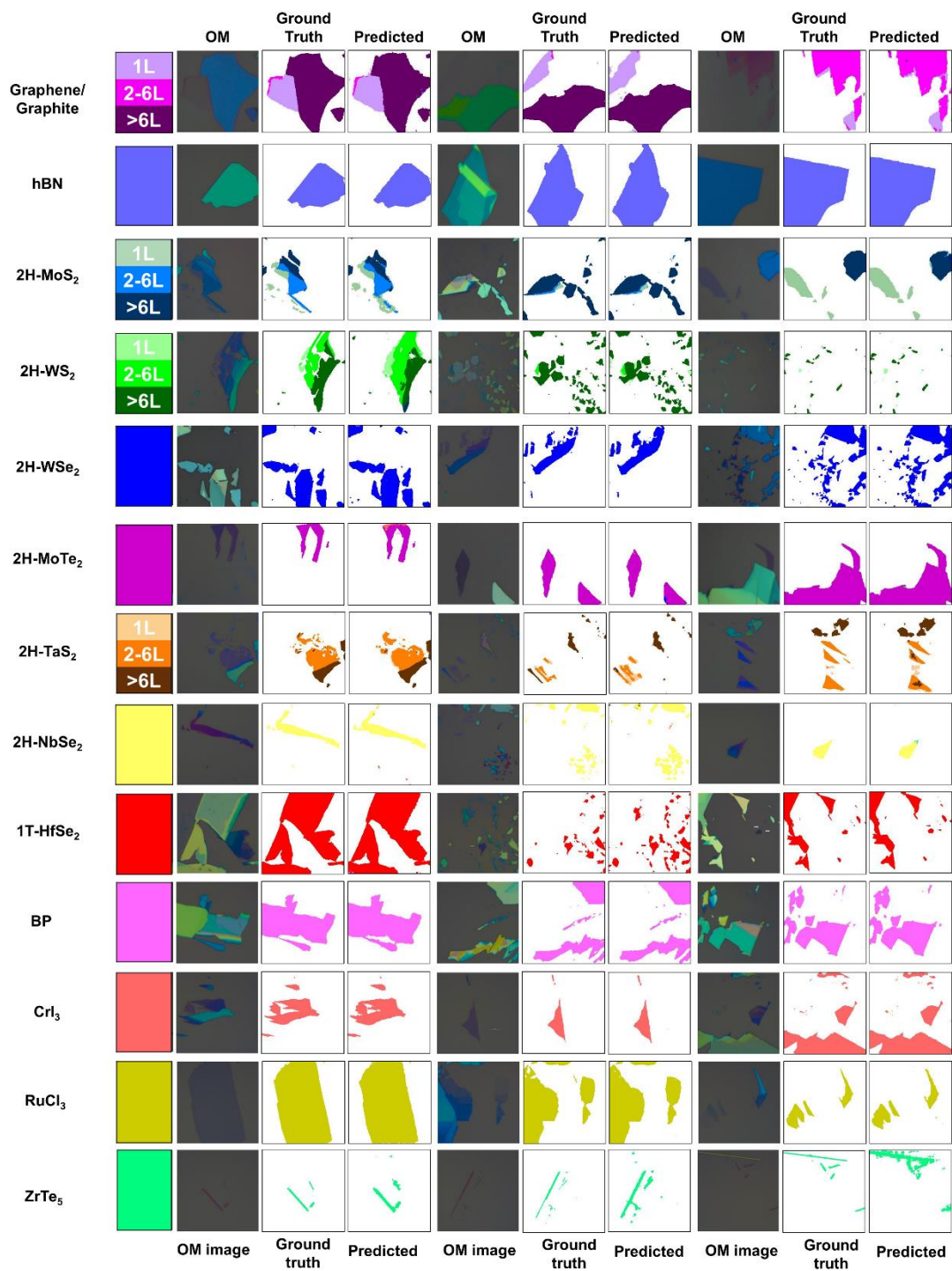


Figure S4. Additional results predicted by the SegNet.

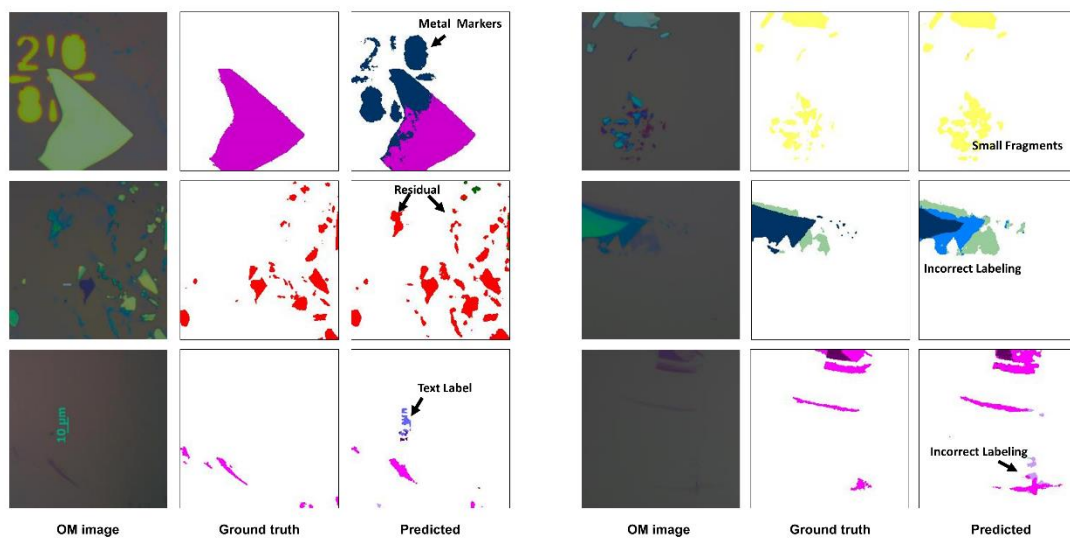


Figure S5. Examples of misclassified images.

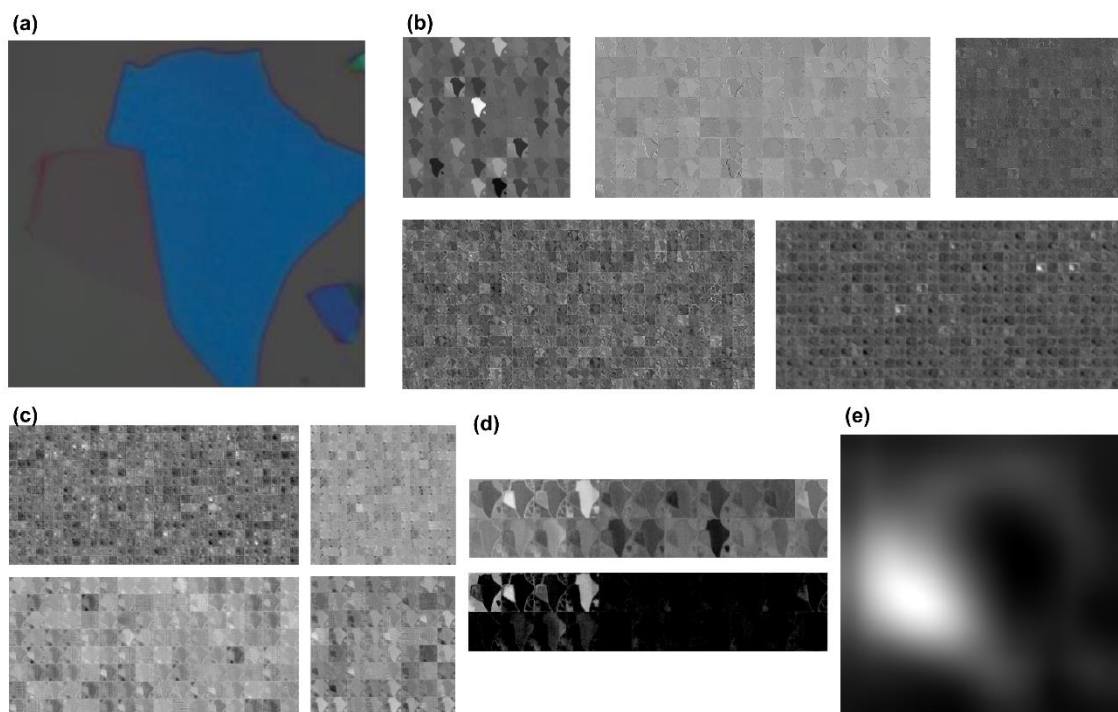


Figure S6. Feature maps in the trained SegNet. (a) the input OM image. (b) Depth=1 to 5 encoder layers. (c) Depth = 5 to 2 decoder layers. (d) The last decoder layers (conv. and ReLU layer). (e) Channel # 153 feature map of the Depth=5 encoder layer.

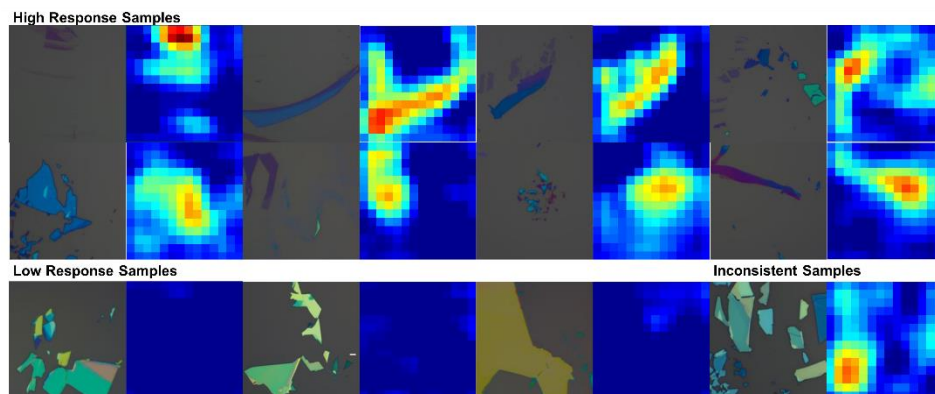


Figure S7. Represented optical images and their corresponding feature maps of Channel #8 of the Depth=5 encoder layer.

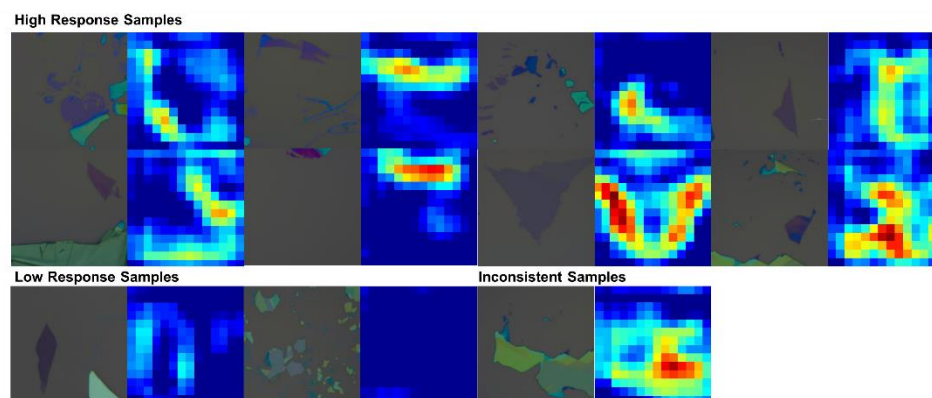


Figure S8. Represented optical images and their corresponding feature maps of Channel #13 of the Depth=5 encoder layer.

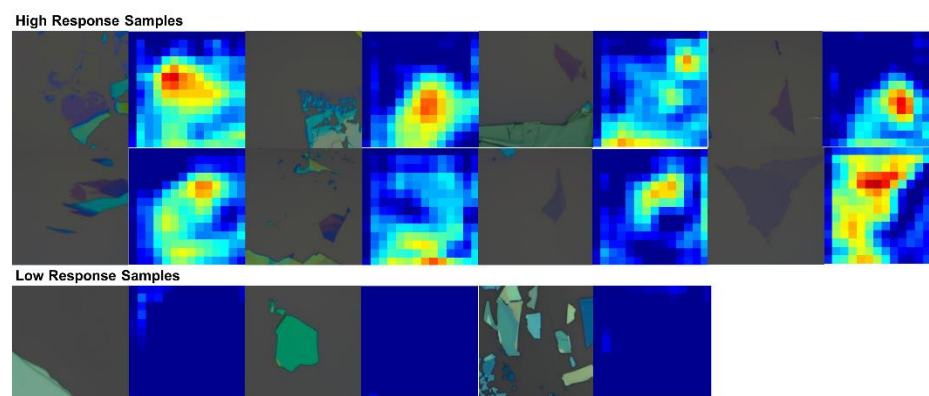


Figure S9. Represented optical images and their corresponding feature maps of Channel #69 of the Depth=5 encoder layer.

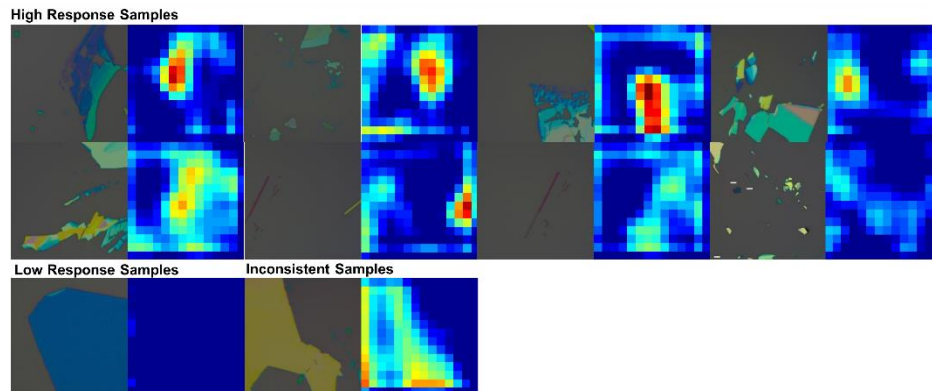


Figure S10. Represented optical images and their corresponding feature maps of Channel #76 of the Depth=5 encoder layer.

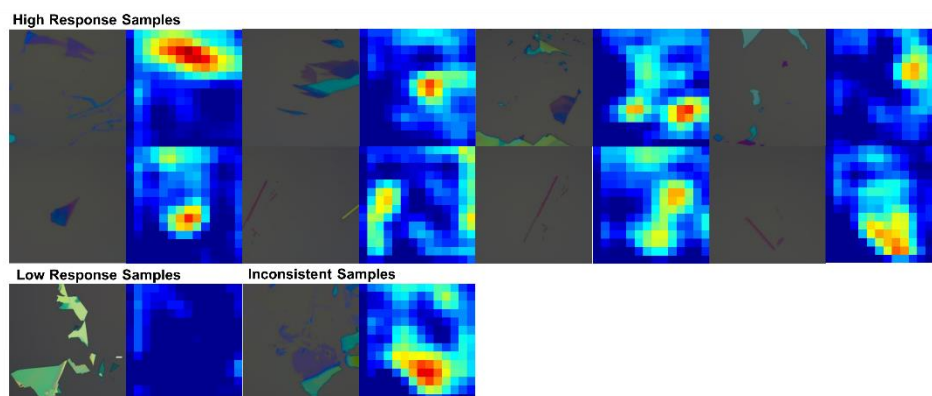


Figure S11. Represented optical images and their corresponding feature maps of Channel #103 of the Depth=5 encoder layer.

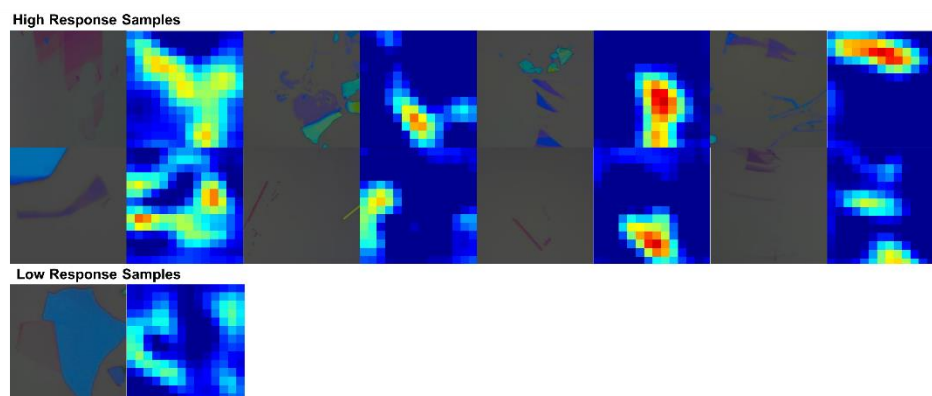


Figure S12. Represented optical images and their corresponding feature maps of Channel #129 of the Depth=5 encoder layer.

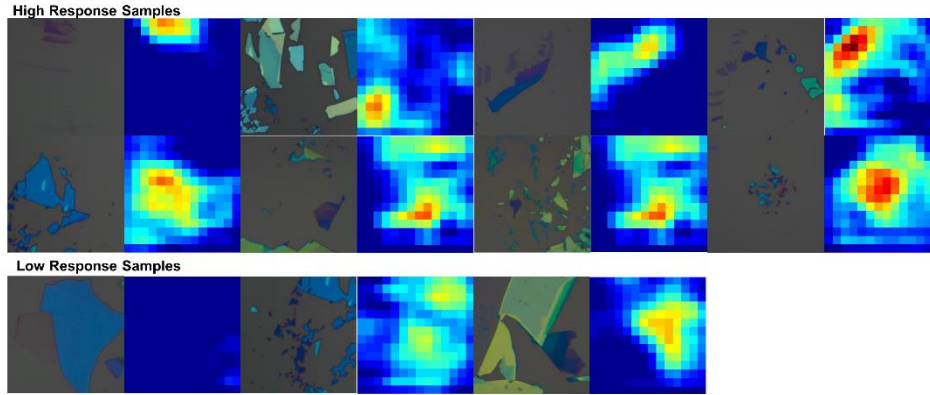


Figure S13. Represented optical images and their corresponding feature maps of Channel #138 of the Depth=5 encoder layer.

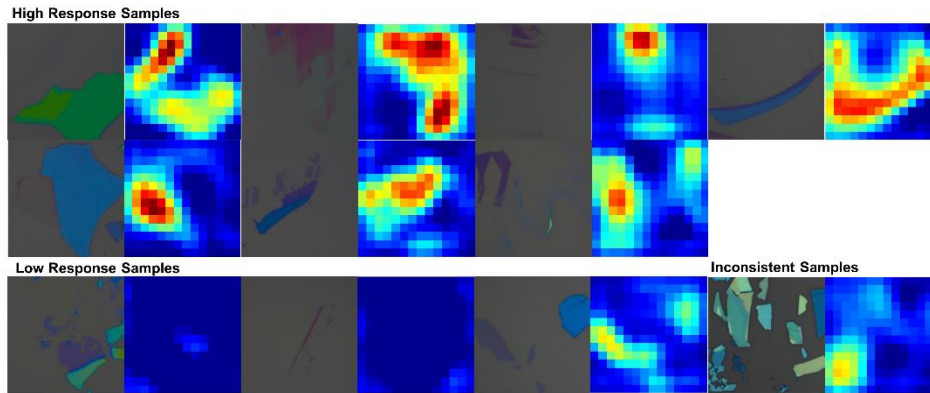


Figure S14. Represented optical images and their corresponding feature maps of Channel #153 of the Depth=5 encoder layer.

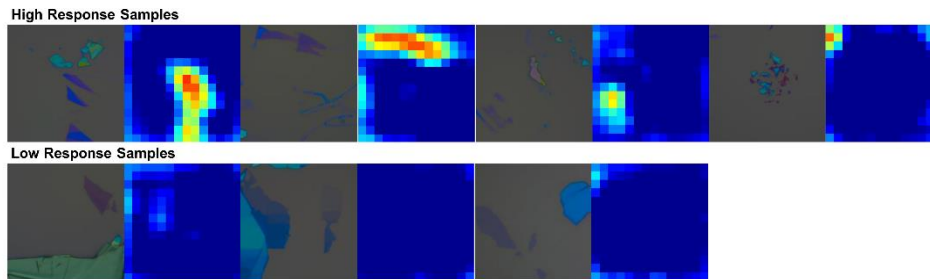


Figure S15. Represented optical images and their corresponding feature maps of Channel #206 of the Depth=5 encoder layer.

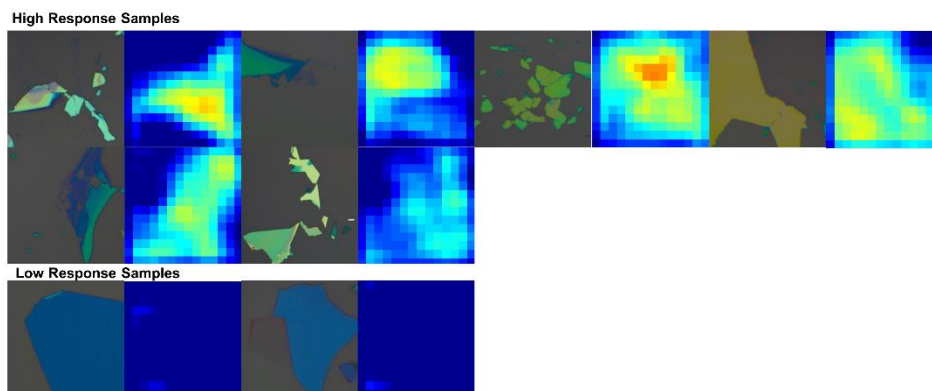


Figure S16. Represented optical images and their corresponding feature maps of Channel #389 of the Depth=5 encoder layer.

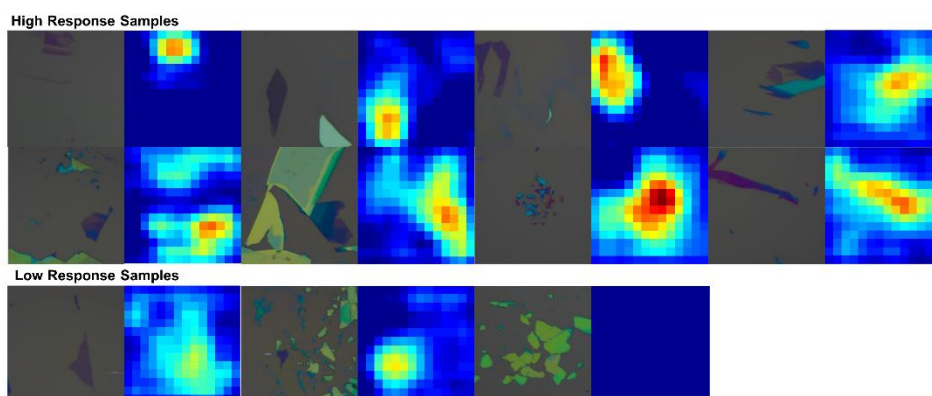


Figure S17. Represented optical images and their corresponding feature maps of Channel #457 of the Depth=5 encoder layer.

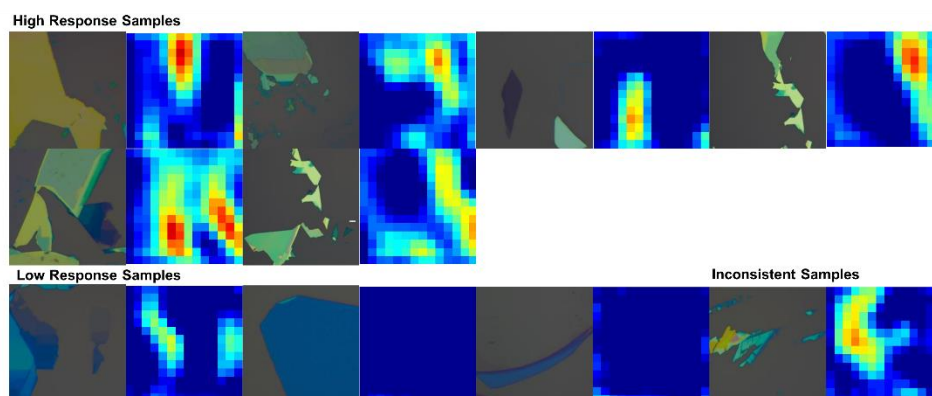


Figure S18. Represented optical images and their corresponding feature maps of Channel #465 of the Depth=5 encoder layer.

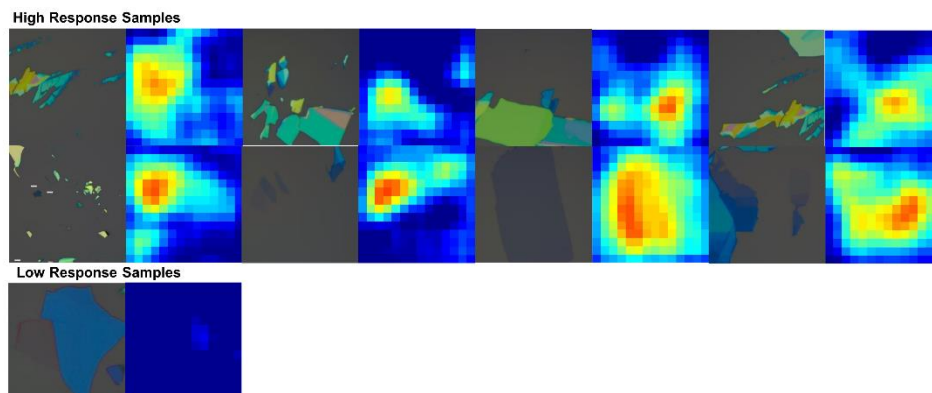


Figure S19. Represented optical images and their corresponding feature maps of Channel #470 of the Depth=5 encoder layer.

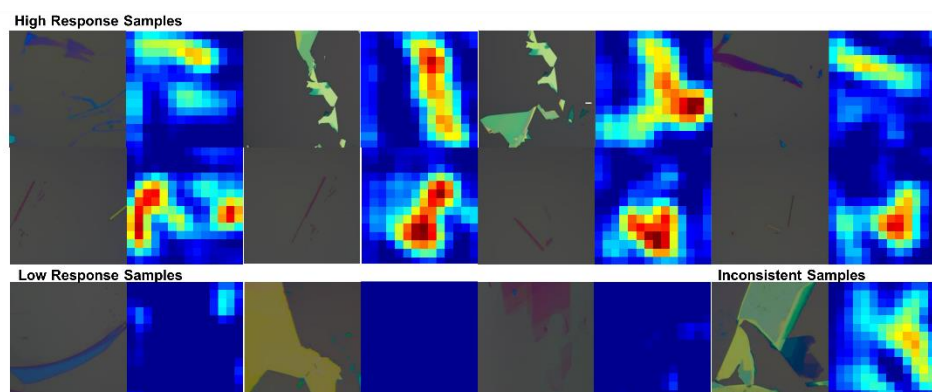


Figure S20. Represented optical images and their corresponding feature maps of Channel #490 of the Depth=5 encoder layer.

Background	0.98	0	0	0	0	0	0	0	0	0	0	0	0	0	0	0	0	0	0	0	0
Graphene monolayer	0.02	0.82	0.16	0	0	0	0	0	0	0	0	0	0	0	0	0	0	0	0	0	0
Graphene fewlayer	0.02	0.32	0.55	0.1	0	0	0	0	0	0	0	0.01	0	0	0	0	0	0	0	0	0
Graphene multilayer	0.01	0	0.08	0.52	0.13	0	0.01	0.17	0	0	0	0.02	0.05	0	0	0	0.01	0	0	0.01	0
hBN	0.04	0	0	0	0.94	0	0	0.01	0	0	0	0	0	0	0	0	0	0	0	0	0
MoS ₂ monolayer	0.06	0	0.01	0	0	0.87	0.03	0	0.02	0.01	0	0	0	0	0	0	0	0	0	0	0
MoS ₂ fewlayer	0.04	0	0.01	0.01	0	0.11	0.64	0.1	0	0.05	0	0.03	0	0	0	0	0	0	0	0	0
MoS ₂ multilayer	0.03	0	0	0.01	0.02	0.01	0.03	0.78	0	0	0.06	0.06	0	0	0	0	0	0	0	0	0
WS ₂ monolayer	0.04	0	0.02	0	0	0.03	0	0	0.58	0.24	0.01	0	0.06	0	0	0	0	0	0	0	0
WS ₂ fewlayer	0.01	0	0	0	0	0.02	0.07	0.01	0.08	0.72	0	0	0.08	0	0	0	0	0	0	0	0
WS ₂ multilayer	0.02	0	0	0	0	0	0.07	0.01	0.01	0.85	0.01	0.04	0	0	0	0	0	0	0	0	0
WSe ₂	0.03	0	0	0.01	0	0	0	0.01	0	0	0	0.9	0.03	0	0	0	0	0	0	0	0
2H-MoTe ₂	0.02	0	0	0.01	0	0	0	0.07	0	0	0.08	0.05	0.73	0	0	0	0	0.01	0	0.02	0
2H-TaS ₂ monolayer	0.1	0	0	0	0	0	0	0	0	0	0	0	0.73	0.16	0	0	0	0	0	0	0.01
2H-TaS ₂ fewlayer	0.02	0	0.02	0.01	0	0	0	0	0	0	0	0.02	0.03	0.77	0.02	0.04	0	0	0	0.07	0
2H-TaS ₂ multilayer	0.01	0	0	0.02	0.03	0	0	0	0	0	0	0	0	0.17	0.55	0	0	0.03	0.14	0.04	0
2H-NbSe ₂	0.03	0	0	0	0	0	0	0	0	0	0	0	0	0.01	0.76	0	0	0.18	0	0.01	0
1T-HfSe ₂	0.04	0	0	0	0	0	0	0	0	0.07	0	0	0	0	0.02	0.81	0.05	0	0	0	0
BP	0.04	0	0	0	0	0	0	0	0	0.07	0	0	0	0	0.03	0	0	0.86	0	0	0
CrI ₃	0.03	0	0	0	0	0	0	0	0	0	0	0	0	0	0.08	0	0	0.87	0.01	0	0
RuCl ₃	0.01	0	0	0	0	0	0	0	0	0	0	0	0	0	0	0.02	0.01	0	0.96	0	0
ZrTe ₅	0.05	0	0	0	0	0	0	0	0	0	0	0	0	0	0	0	0	0	0	0.95	0
2H-MoSe ₂	0.05	0	0	0.09	0.01	0	0	0.02	0	0	0.01	0.26	0.53	0	0	0	0.01	0	0	0.02	0
1T'-MoTe ₂	0.04	0	0	0	0	0.01	0	0.02	0	0.01	0.08	0.03	0.3	0	0	0	0	0.42	0.1	0	0
1Td-WTe ₂	0.1	0	0	0	0	0	0	0.01	0	0	0.36	0	0	0	0	0	0.14	0.33	0.03	0.04	0
ReS ₂	0.15	0	0	0	0	0	0	0.06	0	0.03	0.38	0.01	0.13	0	0	0	0	0.24	0	0	0
SnS ₂	0.11	0	0	0	0.03	0	0	0.01	0	0	0.2	0	0	0	0	0	0	0.65	0	0	0
SnSe ₂	0.12	0	0	0	0.15	0	0	0.05	0	0.01	0.48	0	0.04	0	0	0.01	0	0.13	0	0.01	0
GeSe	0.11	0	0	0	0	0	0	0.01	0	0	0.75	0	0	0	0	0	0	0.13	0	0	0
SnSe	0.13	0	0	0	0	0	0	0	0.01	0.02	0.41	0	0	0	0	0	0.16	0.21	0.04	0	0.02
GaS	0.15	0	0	0	0.27	0	0	0.03	0	0	0.13	0	0	0	0	0.1	0	0	0.31	0	0
CrCl ₃	0.04	0	0	0	0.77	0	0	0	0	0	0	0	0	0	0	0	0	0.13	0	0.05	0
CrBr ₃	0.1	0	0	0	0.25	0.08	0	0	0	0	0	0	0	0	0	0.13	0	0	0.06	0	0.37
MnPS ₃	0.06	0	0	0	0.43	0	0	0	0	0	0.19	0	0	0	0	0.04	0	0	0.28	0	0
FePS ₃	0.11	0	0	0	0.05	0	0	0	0	0	0.07	0	0	0	0	0.24	0	0	0.25	0	0.28
TiS ₃	0.26	0	0	0	0	0	0	0.19	0	0	0.04	0	0	0	0	0	0	0.03	0.47	0	0
ZrS ₃	0.41	0	0	0	0.01	0	0	0.19	0	0	0.22	0	0	0	0	0.03	0	0	0.13	0	0.01
Bi ₄ I ₄	0.47	0	0	0	0	0	0	0	0	0	0	0	0	0	0.01	0.21	0.06	0	0	0.13	0.12
Ta ₂ Se ₈ I	0.37	0	0	0	0	0	0	0	0	0	0.01	0	0.04	0	0	0.02	0.24	0.06	0	0	0.27
Background																					
Graphene monolayer																					
Graphene fewlayer																					
Graphene multilayer																					
hBN																					
MoS ₂ monolayer																					
MoS ₂ fewlayer																					
MoS ₂ multilayer																					
WS ₂ monolayer																					
WS ₂ fewlayer																					
WS ₂ multilayer																					
WSe ₂																					
2H-MoTe ₂																					
2H-TaS ₂ monolayer																					
2H-TaS ₂ fewlayer																					
2H-TaS ₂ multilayer																					
2H-NbSe ₂																					
1T-HfSe ₂																					
BP																					
CrI ₃																					
RuCl ₃																					
ZrTe ₅																					

Figure S21. Extended confusion matrix.

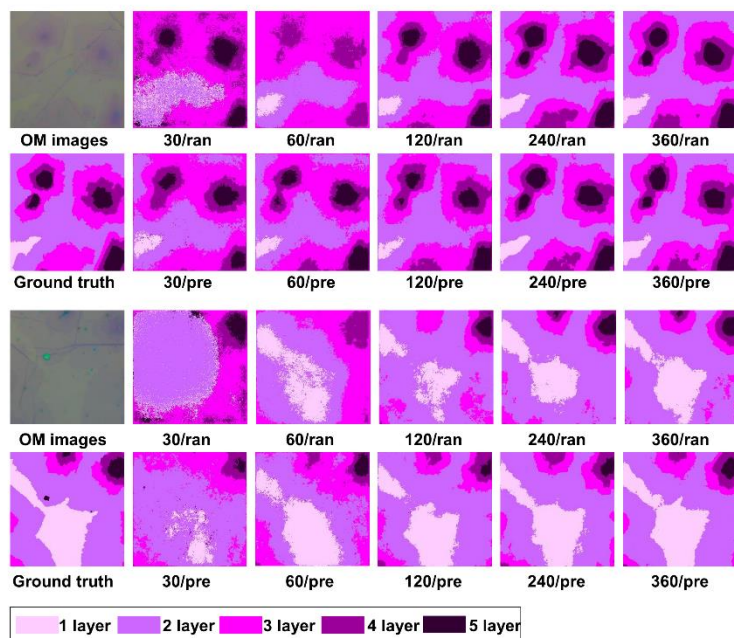


Figure S22. Transfer learning results for CVD graphene. The number of training images are varied from 30 to 360 for both the pretraining method (pre) and the random initialization (ran).

Reference

1. Wilson JA, Yoffe AD. The transition metal dichalcogenides discussion and interpretation of the observed optical, electrical and structural properties. *Advances in Physics* 1969, **18**(73): 193-335.
2. Beal AR, Hughes HP, Liang WY. The reflectivity spectra of some group VA transition metal dichalcogenides. *Journal of Physics C: Solid State Physics* 1975, **8**(24): 4236-4234.
3. McGuire MA, Clark G, Kc S, Chance WM, Jellison GE, Cooper VR, *et al.* Magnetic behavior and spin-lattice coupling in cleavable van der Waals layered CrCl₃ crystals. *Physical Review Materials* 2017, **1**(1): 014001.
4. Lado JL, Fernández-Rossier J. On the origin of magnetic anisotropy in two dimensional CrI₃. *2D Materials* 2017, **4**(3): 035002.
5. Sinn S, Kim CH, Kim BH, Lee KD, Won CJ, Oh JS, *et al.* Electronic Structure of the Kitaev Material α -RuCl₃ Probed by Photoemission and Inverse Photoemission Spectroscopies. *Scientific Reports* 2016, **6**: 39544.

6. Xiong H, Sobota JA, Yang SL, Soifer H, Gauthier A, Lu MH, *et al.* Three-dimensional nature of the band structure of ZrTe₅ measured by high-momentum-resolution photoemission spectroscopy. *Physical Review B* 2017, **95**(19): 195119.
7. Guizzetti G, Nosenzo L, Pollini I, Reguzzoni E, Samoggia G, Spinolo G. Reflectance and thermoreflectance studies of CrCl₃, CrBr₃, NiCl₂, and NiBr₂ crystals. *Physical Review B* 1976, **14**(10): 4622-4629.
8. Zhang K, Deng K, Li J, Zhang H, Yao W, Denlinger J, *et al.* Widely tunable band gap in a multivalley semiconductor SnSe by potassium doping. *Physical Review Materials* 2018, **2**(5): 054603.
9. Burton LA, Whittles TJ, Hesp D, Linhart WM, Skelton JM, Hou B, *et al.* Electronic and optical properties of single crystal SnS₂: an earth-abundant disulfide photocatalyst. *Journal of Materials Chemistry A* 2016, **4**(4): 1312-1318.
10. Evans BL, Hazelwood RA. Optical and electrical properties of SnSe₂. *Journal of Physics D: Applied Physics* 1969, **2**(11): 1507-1516.
11. Molina-Mendoza AJ, Barawi M, Biele R, Flores E, Ares JR, Sánchez C, *et al.* Electronic Bandgap and Exciton Binding Energy of Layered Semiconductor TiS₃. *Advanced Electronic Materials* 2015, **1**(9): 1500126.
12. Kurita S, Staehli JL, Guzzi M, Lévy F. Optical properties of ZrS₃ and ZrSe₃. *Physica B+C* 1981, **105**(1): 169-173.
13. Du K-z, Wang X-z, Liu Y, Hu P, Utama MIB, Gan CK, *et al.* Weak Van der Waals Stacking, Wide-Range Band Gap, and Raman Study on Ultrathin Layers of Metal Phosphorus Trichalcogenides. *ACS Nano* 2016, **10**(2): 1738-1743.
14. Grasso V, Neri F, Perillo P, Silipigni L, Piacentini M. Optical-absorption spectra of crystal-field transitions in MnPS₃ at low temperatures. *Physical Review B* 1991, **44**(20): 11060-11066.
15. Autès G, Isaeva A, Moreschini L, Johannsen JC, Pisoni A, Mori R, *et al.* A novel quasi-one-dimensional topological insulator in bismuth iodide β -Bi₄I₄. *Nature Materials* 2015, **15**: 154.
16. Choudhary K, Cheon G, Reed E, Tavazza F. Elastic properties of bulk and low-dimensional materials using van der Waals density functional. *Physical Review B* 2018, **98**(1): 014107.
17. Zhou J, Shen L, Costa MD, Persson KA, Ong SP, Huck P, *et al.* 2DMatPedia: An open computational database of two-dimensional materials from top-down and bottom-up approaches. *arXiv preprint arXiv:190109487* 2019.